Effect of Different Selenium Precursors on Structural Characteristics and Chemical Composition of $Cu_2ZnSnSe_4$ Nanocrystals

S. Kakherskyi[a,*], R. Pshenychnyi[b], O. Dobrozhan[a], J. Vaziev[b], A. Opanasyuk[a] and Y. Gnatenko[c]

[a] *Sumy State University, Rimsky-Korsakov str., 2, 40007 Sumy, Ukraine*
[b] *Shostka Institute, Sumy State University, 24 Myru Ave., 41600 Shostka, Ukraine*
[c] *Institute of Physics of National Academy of Sciences of Ukraine, 03028 Kyiv, Ukraine*

Received: 27.10.2021 & Accepted: 08.02.2022

Doi: 10.12693/APhysPolA.141.487 *e-mail: s.kacherski@ekt.sumdu.edu.ua

In this work, $Cu_2ZnSnSe_4$ nanocrystals were synthesized by the polyol method. The chemical composition and morphological, structural, and microstructural properties of $Cu_2ZnSnSe_4$ nanocrystals, depending on the synthesis temperature and time, as well as the composition of the precursor, have been thoroughly investigated using scanning and transmission electron microscopy, energy dispersive X-ray analysis, X-ray diffraction, FTIR spectroscopy, Raman spectrometry, and low-temperature photoluminescence. We compared the properties of nanocrystals synthesized from different precursors containing selenourea or amorphous selenium as a source of selenium and then determined the optimal conditions for the synthesis of nanocrystals. It was found that the optimal synthesis time for nanocrystals obtained in the first approach is $\tau = 30$–45 min, and in the second approach — $\tau = 120$ min. It was also found that the optimal composition for the synthesis of single-phase $Cu_2ZnSnSe_4$ nanocrystals in the second approach is the molar ratio of precursors 2:1.5:1:4, and the synthesis temperature $T = 280$°C. Thus, $Cu_2ZnSnSe_4$ nanocrystals synthesized under optimal conditions are used to develop nanoinks for printing solar cell absorbers by two- and three-dimensional printers.

topics: nanocrystals, $Cu_2ZnSnSe_4$, chemical composition, morphology

1. Introduction

Research topics related to the development of electronic elements and devices using two- (2D) and three-dimensional (3D) printing techniques are advancing rapidly so far. These techniques are affordable, versatile, economical and waste-free, which can significantly simplify the manufacturing process and reduce production costs [1–3]. In addition, it is possible to use a wide range of substrates, including flexible ones, because such technologies are low-energy and do not require heating the substrates up to thermal degradation [4–10].

Simple inkjet printers, in which standard inks can be replaced by nanoinks containing a suspension of metals or semiconductor nanocrystals (NCs), can be used for the 2D printing of electronic elements and devices [11–13]. Three-dimensional printers allow us to print films on substrates of any shape, including human skin or clothing [4, 14–19].

Two-dimensional and three-dimensional printing technologies with nanoinks based on metal NCs allow the development of printed circuit boards [20, 21] and the use of various semiconductor compounds for the design of passive and active elements of electronic devices [22–29]. However, the scientific and technological challenge nowadays is to develop a procedure for the synthesis of semiconductor NCs with controlled properties and to develop stable and environmentally friendly colloidal solutions with the required surface tension and viscosity, which can be used as inks for ink printing processes [30–32].

Nowadays, solar cells (SCs) based on bulk silicon monocrystals and polycrystals (first generation SC) and films of direct-gap elements GaAs, InP, $Ga_xIn_{1-x}P$, CdTe, $CuInSe_2$ (CIS), and $CuIn_{1-y}GaySe_2$ (CIGS) (second generation SC), can be replaced by those made of new materials [33–35], devoid of the shortcomings of previous ones. For the creation of SCs absorbers of the third generation, it is proposed to use multicomponent compounds Cu_2ZnSnS_4, $Cu_2ZnSnSe_4$, and $Cu_2ZnSn(S_xSe_{1-x})_4$ with a kesterite structure [36–40]. These compounds possess close to the optimal energy bandgap (E_g), high light absorption coefficient ($\sim 10^5$ cm^{-1}), long lifetime, and high mobility of charge carriers [41]. Kesterite-based compounds do not contain rare and environmentally hazardous components, on the contrary, their

elements are widespread in the earth's crust, and the cost of their production is low [42, 43]. However, today, the efficiency of SCs based on these materials does not exceed 10.0–11.3% [44]. Note that the most efficient SCs absorbers ($\eta = 11.1\%$) were obtained by the vacuum-free method using a hydrazine-based solution [45]. Hydrazine used as a solvent in such a process is highly toxic, requires very careful handling, and cannot be used in mass production.

One of the reasons for the low efficiency of SCs based on the Cu_2ZnSnS_4, $Cu_2ZnSnSe_4$, and $Cu_2ZnSn(S_xSe_{1-x})_4$ layers is the narrow range of homogeneity of the compounds, which causes the appearance of a large number of defects and secondary phases during the growth of the thin films and, as a result, its low structural quality. Therefore, an effective strategy to obtain thin films of kesterite compounds with a controlled crystal structure and chemical composition, high degree of crystallinity, and minimal content of secondary phases, is processing them in three stages. These are (i) colloidal synthesis of single-phase NCs, (ii) subsequent deposition of its suspension on substrates using non-vacuum methods, for example, spray methods or 2D and 3D printing techniques, and finally, (iii) post-growth thermal annealing of the obtained samples to improve structural properties [36, 46]. As a result, the structural properties of thin films, such as phase composition, lattice parameters, and size of coherent scattering regions (CSRs), which play an important role in determining the functional characteristics of SCs, depend mainly on the conditions of obtaining NCs and their post-growth treatment. SCs with solar energy conversion efficiency $\eta = 10.2\%$ were obtained on the basis of the $Cu_2ZnSn(S_xSe_{1-x})_4$ absorbers grown from initial $Cu_2ZnSnSe_4$ NCs [43]. However, $Cu_2ZnSn(S_xSe_{1-x})_4$ films are now mainly made from Cu_2ZnSnS_4 nanocrystals [47, 48], not $Cu_2ZnSnSe_4$, because Cu_2ZnSnS_4 NCs are easier to obtain compared to $Cu_2ZnSnSe_4$ NCs. Currently, selenourea $(NH_2)_2CSe$ is used mainly as a source of selenium in the synthesis of $Cu_2ZnSnSe_4$ and $Cu_2ZnSnSe_4$ nanocrystals [49–51]. When precursors based on cheaper elemental selenium $Cu_2ZnSnSe_4$ were used, NCs were obtained only by the solvothermal method [52, 53], the hydrothermal method [54], the two-step hot-injection method [55, 56], and the solvent-thermal reflux technique [57, 58].

Previously, we optimized the conditions for the synthesis of Cu_2ZnSnS_4 and ZnO NCs using the polyol method [59–63]. As a result, we obtained single-phase nanocrystals of the kesterite (CZTS) and wurtzite (ZnO) phases with controlled sizes, respectively. In this work, we optimize the process of $Cu_2ZnSnSe_4$ NCs synthesis using two different sources of selenium in the precursor selenourea and elemental selenium. Next, we investigate the morphological, structural, and microstructural properties depending on the synthesis temperature, time, and precursor combination.

2. Materials and methods

$Cu_2ZnSnSe_4$ NCs were synthesized by the polyol method in the reaction medium of diethylene glycol (DEG) and triethylene glycol (TEG) using two different selenium precursors.

In *the first approach*, a solution of polyvinylpyrrolidone (PVP) in a mass ratio of 1:1 to the finished product was initially prepared. Then a mixture of $CuCl_2{\cdot}2H_2O$, $Zn(CH_3COO)_2{\cdot}2H_2O$, and $SnCl_2{\cdot}2H_2O$ salts in the different Cu:Zn molar ratios, was added to the resulting solution, which was then heated to 65°C and stirred with a magnetic stirrer for one hour. The synthesis of NCs at the reaction medium temperature was carried out separately with the exposure interval $\tau = 0$, 15, 30, and 60 min. More details on the synthesis procedure are described in [63].

In *the second approach*, a mixture of the $CuCl_2{\cdot}2H_2O$, $Zn(CH_3COO)_2{\cdot}2H_2O$, and $SnCl_2{\cdot}2H_2O$ salts, as well as amorphous selenium grounded in an agate mortar, were placed in a 50 ml three-necked flask. Then 12 ml of TEG was added with subsequent heating, as described in the first approach. Contrary to the first approach, where selenourea is used as a source of selenium, i.e., $(NH_2)_2CSe$ compound [64–67], the use of elemental selenium allowed us to reduce the cost of synthesizing the final compound significantly. Upon reaching a temperature of 120°C, the air was pumped out of the flask, and inert argon gas was charged. The mixture was kept at this temperature for 30 min and then quickly heated to the synthesis temperatures $T = 220$, 240, 250, 260, 270, and 280°C for 120 min. In the process of the synthesis of $Cu_2ZnSnSe_4$ NCs, samples with the exposure interval $\tau = 30$, 60, 90, and 120 min were obtained at the reaction medium temperature of 260°C. The initial molar ratio of elements in the precursors used corresponded to the stoichiometric composition of the compound (2:1:1:4), and the amount of zinc was exceeded.

In both the first and second approaches, after synthesis, the mixture was cooled down to room temperature, and the synthesized product was separated from the organic component (DEG, TEG) by centrifugation. The residue of polyol compounds was washed using ethanol while shaking vigorously and then centrifuged. The washed $Cu_2ZnSnSe_4$ samples were dried at 60°C for 12 h.

X-ray diffractometer DRON 4-07 was used to determine the structural and microstructural properties of the synthesized NCs. The analysis was carried out using Ni-filtered K_α radiation on the copper anode. The obtained diffractograms were normalized to the peak intensity (112) of the tetragonal phase of the $Cu_2ZnSnSe_4$ compound. The phase analysis was performed by comparing the diffraction angles from the test samples and the diffraction angles according to the reference data of JCPDS ($Cu_2ZnSnSe_4$ — No.00-052-0868 [67]).

All profile lines were processed to the following procedures: background extraction, emission smoothing, and separation of K_α double, which were performed using standard diffractometer software.

The lattice parameters a and c of a tetragonal unit cell were calculated using the following equations [68, 69]

$$a_{\mathrm{CZTS}} = \frac{\lambda}{2\sin(\theta)}\sqrt{h^2+k^2+l^2\left(\frac{a}{c}\right)^2}, \tag{1}$$

$$c_{\mathrm{CZTS}} = \frac{l}{\sqrt{-\frac{h^2+k^2}{a^2}+\left(\frac{2\sin(\theta)}{\lambda}\right)^2}}, \tag{2}$$

where 2θ is the Bragg angle, λ is the wavelength of X-ray radiation, and (hkl) are the Miller indices. The reflection from the crystallographic plane (112) was used for the calculations. The unit volume of materials was calculated using the formula $V_{\mathrm{unit}} = a^2\,c$ [65–67]. Also, we used the UnitCell program to calculate lattice parameters of material [68–70].

The average size of CSR and the level of microdeformations (ε) in the obtained samples were calculated by physical broadening of the diffraction peaks (112), (204), (312). The following equations were used [68–71]

$$L = \frac{0.94\lambda}{\beta\cos(\theta)}, \tag{3}$$

$$\varepsilon = \frac{\beta\,\cos(\theta)}{4}, \tag{4}$$

where λ is the wavelength, β is the extension of the corresponding diffraction maximum, and θ is the diffraction angle.

The morphological properties of the synthesized NCs were studied using a transmission electron microscope TEM-125K. The study of NCs elemental composition was performed using a scanning electron microscope SEO-SEM Inspect S50-B equipped with an energy-dispersive spectrometer AZtecOne with X-MaxN20 detector (Oxford Instruments plc).

Raman spectra studies from NCs were performed using a Renishaw inVia Reflex microspectrometer at room temperature. Two solid-state lasers with a radiation wavelength $\lambda = 532$ nm and $\lambda = 785$ nm and maximum output power of at least 50 mW were used as the source of the excitation radiation.

To study the photoluminescence (PL) spectra of NCs, equipment based on a bright spectrophotometer with a double monochromator SDL-1 was used. The excitation of PL was performed using the CUD 7GF1B LED with maximum radiation of 274 nm and LEDs with a wavelength of 620 nm. To establish and stabilize temperature of the sample, the UTREX system was used, which allowed for temperature stabilization with an accuracy of 0.01 K.

The methodology for studying the structural, microstructural and chemical properties of nanomaterials has been described in detail in our previous works [60, 62, 69–72].

3. Results and discussion

3.1. Structural and microstructural characteristics of CZTSe nanocrystals and thin films

3.1.1. Morphology and local chemical analysis

Electron microscopic images of $Cu_2ZnSnSe_4$ NCs synthesized at different growth times using the first and second approaches are shown in Fig. 1. It was found that the average size of NCs synthesized by the first method show an increase from 5.0 ± 3.0 nm ($\tau = 30$ min) to 12.0 ± 3.0 nm ($\tau = 60$ min). The NCs sizes obtained by the second method were two to three times larger than those obtained by the first method. The crystals showed different shapes, i.e., from quasi-spherical to pyramidal forms. During the synthesis process, NCs collected in conglomerates with sizes 50–80 nm (Fig. 1).

To determine the optimal conditions for the obtained NCs, we investigated the dependence of the phase composition on temperature, synthesis time, and precursor composition. Figure 2 presents diffractograms from NCs, in the synthesis of which the $(NH_2)_2CSe$ compound was used (first approach). The particles were obtained during the synthesis time from 0 to 60 min. Diffraction patterns from NCs show reflection peaks at 27.25–27.30°, 45.30–45.35°, 53.60–53.65°, 65.85–66.40°, and 72.65–72.75°, which correspond to the reflections from (112), (204), (312), (008), and (316) crystallographic planes of the $Cu_2ZnSnSe_4$ compound of the tetragonal phase. Secondary phases in the material were not detected by the XRD method, because its concentration did not exceed the detection level of the method (3–5% by weight) [72]. Diffractograms of the $Cu_2ZnSnSe_4$ NCs synthesized using the first approach can be characterized by the following features: (i) with increasing synthesis time, the intensity of diffraction peaks increases

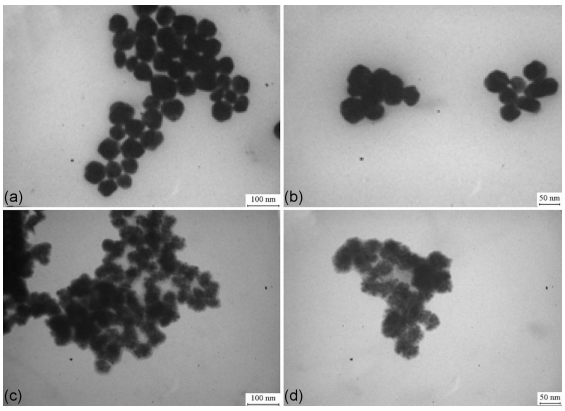

Fig. 1. Electron microscopic images of $Cu_2ZnSnSe_4$ NCs conglomerates obtained using Se (composition 2:1.5:1:4, T=280°C, τ=120 min) (a,b) and $(NH_2)_2CSe$ (composition 2:1:1:4, T=240°C, τ=30 min) (c,d).

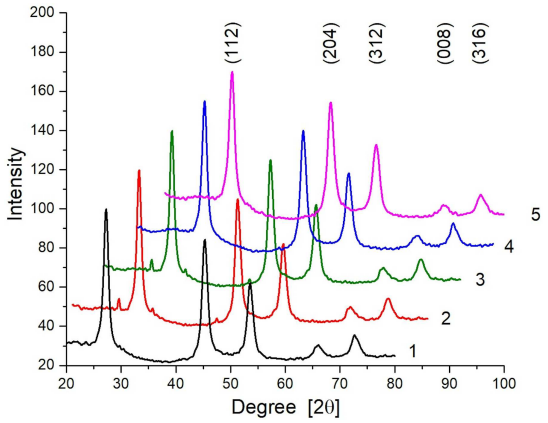

Fig. 2. Diffractograms of $Cu_2ZnSnSe_4$ NCs synthesized using $(NH_2)_2CSe$ at $T = 240$°C for a given time τ=0 min (curve 1), 15 (curve 2), 30 (curve 3), 45 (curve 4), and 60 (curve 5).

significantly (e.g., for the plane (112) in the synthesis time 0–60 min, the peak intensity doubles) and (ii) the half-width of diffraction peaks decreases.

In the case of syntheses using elemental selenium (the second approach), the exposure interval of the reaction medium at different temperatures was 120 min. The initial molar ratio of the precursors used corresponded to the stoichiometric composition of the compound and was $CuCl_2$:$Zn(CH_3COO)_2$:$SnCl_2$:Se = 2:1:1:4. The diffractograms obtained from the synthesized NCs are shown in Fig. 3a. As can be seen at the synthesis temperature of 220°C, the diffraction patterns from NCs show a large number of lines, indicating that there is a mixture of different phases (curve 1). According to [73], in the case of zinc-depleted material, Cu_2SnSe_3, $Cu_2ZnSn_3Se_8$, Cu_2Se, and Cu_4SnS_4 compounds can be formed. These compounds are characterized by the presence of several polymorphic modifications. But the main feature that complicates the more accurate interpretation of the results of the X-ray phase analysis is that these phases have spectra very similar to the diffraction spectra of the $Cu_2ZnSnSe_4$ compound of the tetragonal phase [74–77].

It is established that with increasing synthesis temperature, the number of peaks in the diffraction patterns decreases (curves 2 and 3). At $T \geq 260$°C in the reaction medium, a product or mixture of products with almost the same position of peaks and their intensity ratio (curves 4–6) was formed.

The diffractograms of the substance synthesized at $T \geq 260$°C show the reflection peaks at 27.05–27.30°, 45.00–45.25°, 53.30–53.60°, 65.60–65.90°, and 72.35–72.70°, corresponding to the reflections from (112), (204), (312), (008) and (316) crystallographic planes of the $Cu_2ZnSnSe_4$ compound. Secondary phases in the material were not detected by the diffractometric method.

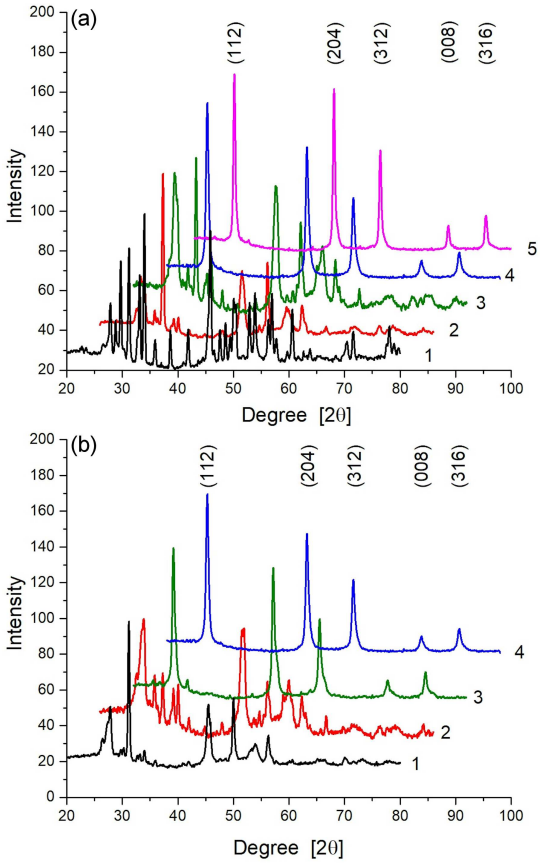

Fig. 3. Diffractograms of $Cu_2ZnSnSe_4$ NCs synthesized using elemental selenium for a given time τ=120 min at different temperatures T = 220°C (1), 240 (2), 250 (3), 260 (4), 270 (5), and 280 (6) (a); and for a given time τ= 30 min (1), 60 (2), 90 (3), and 120 (4) at temperature $T = 260$°C (b).

To determine the optimal conditions for the synthesis of NCs at 260°C, at which a material single-phase is formed, samples were taken at different exposure times of the reaction mixture. The corresponding diffractograms from the samples synthesized over time τ = 30, 60, 90, and 120 min are shown in Fig. 3b. The results indicate that the optimal NCs synthesis interval was 120 min (curve 4).

To determine the chemical composition of the obtained material, its chemical analysis was performed using the EDX method. It is known that the theoretical atomic ratio of the components of the $Cu_2ZnSnSe_4$ compound must be $C_{Cu} : C_{Zn} : C_{Sn} : C_{Se} = 25.0 : 12.5 : 12.5 : 50.0$ (Table I). The content of the components of the compound in the precursor was selected accordingly. When determining the composition of the samples, it was observed that the entry of different elements into NCs occurs at different speeds. So, at the synthesis temperature T = 260°C and the time of 30 min, zinc atoms are not embedded from the reaction medium into the compound (Table I). In this case, the CuSe and Cu_2SnSe_3 phases are formed in the sediment

TABLE I

The elementary composition of $Cu_2ZnSnSe_4$ NCs obtained by the second approach from precursors of different composition under alteration of the synthesis conditions.

Samples		Atomic percentage				Relation	
T [°C]	τ [min]	C_{Cu}	C_{Zn}	C_{Sn}	C_{Se}	$C_{Cu}/N_{(Zn+Sn)}$	C_{Zn}/C_{Sn}
$Cu_2ZnSnSe_4$ 2:1:1:4							
260	30	45.3	0	9.3	45.4	4.87	0
260	60	33.6	1.6	15.5	49.4	1.97	0.10
260	90	35.6	1.5	15.1	47.8	2.15	0.10
260	120	35.8	2.0	15.8	46.4	1.97	0.13
270	120	41.0	3.8	13.3	41.9	2.40	0.29
280	120	33.3	8.2	12.9	45.7	1.58	0.64
$Cu_2ZnSnSe_4$ 2:1.5:1:4							
280	120	29.0	12.1	12.7	46.2	1.17	0.95
$Cu_2ZnSnSe_4$ 2:1.8:1:4							
280	120	32.7	11.0	13.2	43.2	1.35	0.83
stoichiometric composition		25.0	12.5	12.5	50	1.00	1.00
optimal for the creation of SC composition		22.22	14.55	13.23	50	0.80–0.85	1.10–1.20

in a ratio of 2:1, which is confirmed by the X-ray diffractometry data. With the growth time of NCs increasing to 120 min, the zinc content in the synthesized product increases to 2 at.%.

It was found that with the increase in the synthesis temperature, the amount of zinc in the samples gradually increases, being 3.8 at.% for 270°C and 8.2 at.% for 280°C. Hence, the increasing synthesis temperature promotes the entry of zinc atoms into the final product. Since the experimentally obtained ratio of constituent atoms in the material is nonstoichiometric, it can be assumed that the obtained product still consists of several phases.

To obtain a single-phase product during synthesis at 280°C for 120 min, the concentration of zinc in the reaction medium was increased by 1.5 to 1.8 times. The results of the X-ray phase analysis showed that the spectra from the samples were similar to the spectra previously obtained (Fig. 4), which are characteristic to single-phase samples.

The analysis of the results obtained by the EDAX method (Table I) showed that the optimal composition for the $Cu_2ZnSnSe_4$ synthesis is the molar ratio of 2:1.5:1:4. In this case, the formed product was the closest (C_{Cu}=29.0 at.%, C_{Zn}=12.1 at.%, C_{Sn}=12.7 at.%, C_{Se}=46.2 at.%) to the stoichiometric composition (C_{Cu}=25.0 at.%, C_{Zn}=12.5 at.%, C_{Sn}=12.5 at.%, C_{Se} = 50.0 at.%). With a further increase in the proportion of zinc in the reaction mixture to 1.8, the content of copper and tin in the samples increased to 32.7 and 13.2 at.%, respectively, with a simultaneous decrease in the final synthesis product, namely, zinc and selenium decreased to 11.0 and 43.2 at.%, respectively (Table I).

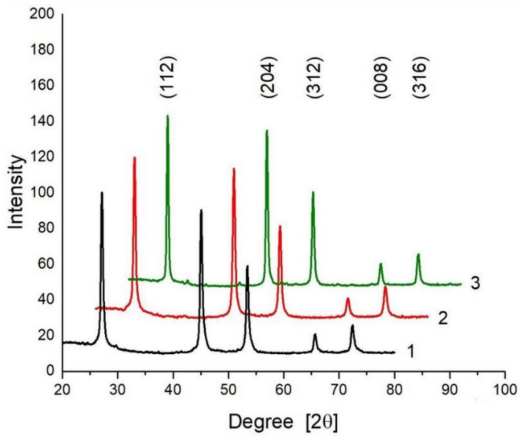

Fig. 4. Diffractograms of $Cu_2ZnSnSe_4$ NCs synthesized at T = 280°C, τ = 120 min for nonstoichiometric precursors 2:1:1:4 (1), 2:1.5:1:4 (2), 2:1.8:1:4 (3).

To establish the influence of growth time on the structural and substructural characteristics of $Cu_2ZnSnSe_4$ NCs, we determined the sizes of coherent scattering regions (L), the level of microdeformations (ε), and the lattice parameters (a, c, c/a, $V_{\text{unit.}}$). Their values are given in Table II. There are also reference values of the lattice constants of the studied compounds.

Lattice parameters of semiconductor materials are extremely sensitive to the introduction of impurities, changes in stoichiometry, and oxidation, so the exact values of these parameters allows us to study the relevant processes. Table II shows the obtained values of $Cu_2ZnSnSe_4$ NCs lattice

TABLE II

The structural and microstructural properties of $Cu_2ZnSnSe_4$ NCs synthesized by different approaches. The value of $a = 0.56930$ nm, $c = 1.13330$ nm, $n/2a = 0.99535$, and $V_{eii} = 0.3673$ nm^3 (according to the reference data JCPDS No. 00-026-0575 [67]).

Samples			$L_{(112)}$	$L_{(204)}$	$L_{(312)}$	$\varepsilon_{(112)}$	$\varepsilon_{(204)}$	$\varepsilon_{(312)}$	$a_{(112)}$, a_{UC}	$c_{(122)}$, c_{UC}	$c_{(122)}/2a_{(122)}$, $c_{UC}/2a_{UC}$	$V_{\text{unit}\,(112)}$, $V_{\text{unit}\,(UC)}$
T [°C]	τ [min]	Precursor composition	[nm]	[nm]	[nm]	($\times 10^3$)	($\times 10^3$)	($\times 10^3$)	[nm]	[nm]		[nm^3]
NCs synthesized by the first approach												
240	0	2:1:1:4	4.47	4.77	4.72	8.16	7.69	7.79	0.56624, 0.56739	1.11545, 1.12621	0.9850, 0.99245	0.3576, 0.3626
240	15	2:1:1:4	7.29	6.19	5.82	5.02	5.94	6.34	0.56624, 0.56619	1.11545, 1.13345	0.9905, 1.0009	0.3576, 0.3634
240	30	2:1:1:4	8.10	6.90	6.55	4.53	5.34	5.64	0.56726, 0.56777	1.12134, 1.12839	0.9952, 0.9937	0.3608, 0.3638
240	45	2:1:1:4	8.36	7.27	6.95	4.40	5.08	5.32	0.56726, 0.56695	1.12134, 1.13165	0.9884, 0.9980	0.3608, 0.3638
240	60	2:1:1:4	9.03	7.51	7.05	4.07	4.92	5.24	0.56624, 0.56605	1.11545, 1.13298	1.0070, 1.0008	0.3576, 0.3630
NCs synthesized by the second approach												
260	120	2:1:1:4	16.54	15.08	14.32	2.27	2.50	2.64	0.56624, 0.56645	1.11545, 1.13290	0.9849, 1.0000	0.3576, 0.3635
270	120	2:1:1:4	21.17	20.99	20.91	1.77	1.82	1.84	0.56829, 0.56802	1.12732, 1.13600	0.99185, 0.9999	0.3641, 0.3665
280	120	2:1:1:4	20.22	19.39	18.68	1.85	1.96	2.05	0.56931, 0.56820	1.13338, 1.13611	0.9954, 0.9997	0.3673, 0.3668
280	120	2:1.5:1:4	19.61	18.54	17.68	1.90	2.05	2.16	0.57138, 0.56925	1.14577, 1.13760	1.0026, 0.9992	0.3741, 0.3686
280	120	2:1.8:1:4	24.23	22.95	21.23	1.55	1.67	1.81	0.57138, 0.56956	1.14577, 1.13741	1.0026, 0.9985	0.3741, 0.3690

parameters calculated using the relations (1)–(2) for reflections from the crystallographic plane (112) and the UnitCell program. It was found that the values of the lattice parameters found by two different methods differ quite significantly in magnitude. The general form of the dependence of a, c, $c/(2a)$, V_{unit} on T, τ and the precursors composition was very similar. Since the results obtained using the UnitCell program are based on the analysis of all reflections presented on the diffractograms of the samples, they are more accurate. Therefore, only this data will be discussed.

The analysis of the results of diffractometric studies shows that the lattice parameters of nanocrystals synthesized by the first method vary in the following range: $a_{\text{UC}} = 0.56605$–0.56777 nm, $c_{\text{UC}} = 1.12621$–1.13345 nm, $c_{\text{UC}}/(2a_{\text{UC}}) = 0.99245$–$1.0009$. Initially, with as the synthesis time increases, the value of a increases to the maximum (a_{UC}=0.56777 nm at τ=30 min), and then decreases to the minimum ($a_{\text{UC}} = 0.56605$ nm at $\tau = 60$ min). The material of NCs synthesized at τ=45 min (a_{UC}=0.56695 nm) had parameters closest to the reference data ($a_{\text{UC}} = 0.56930$ nm).

At the same time, the value of the lattice parameter c increases with the increase in synthesis time of NCs, reaching at τ=60 min (c_{UC}=1.13298 nm) values typical for stoichiometric materials ($c_{\text{UC}} = 1.13330$ nm) [72–74]. A similar increase is observed in the ratio of the quantities $c_{\text{UC}}/(2a_{\text{UC}})$, which at the synthesis time $\tau = 45$–60 min begins to exceed the reference data. Simultaneously, the calculated unit cell volume of the compound ($V_{\text{unit(UC)}} = 0.3626$–$0.3638$ nm^3) turned out to be less than the reference value ($V_{\text{unit(UC)}} = 0.3673$ nm^3) in the overall range of synthesis times.

In the case of NCs synthesized by the second method, there was a tendency to increase such lattice parameters as a_{UC}, c_{UC}, $V_{\text{unit(UC)}}$ by increasing the synthesis temperature and the zinc content in the precursor — at the same time value of relation $c_{\text{UC}}/(2a_{\text{UC}})$ decreases (Table II).

The results of determining the size of CSR, L, and the level of microdeformations, ε, obtained by a physical broadening of the diffraction peaks (112), (204), and (312) in $Cu_2ZnSnSe_4$ NCs are shown in Table II. Analysis of these results shows that with the increase in the synthesis time, the CSR sizes of $Cu_2ZnSnSe_4$ NCs synthesized by the first method increase from 4.47 nm ($\tau = 0$ min) to 9.03 nm ($\tau = 60$ min) in the [112] direction. Similar, albeit somewhat smaller, increase in L occurs in two other directions [204] and [312]. At the same time, taking into account the accuracy of the method, the form of CSR is close to spherical.

The CSR sizes of NCs synthesized by the second method turned out to be much larger than that of the first method, and vary in the range

$L_{(112)}$ = 16.54–24.23 nm. There was also a tendency in nanocrystal CSR sizes to increase with an increase in the synthesis temperature and the amount of zinc in the precursor. A similar process was observed for L in the directions [204] and [312]. As in the first case, the CSR sizes were close to the spherical form. It should be noted that the CSR sizes practically coincided with the NCs sizes determined using transmission electron microscopy (Fig. 2). This suggests that nanocrystals usually consist of one single CSR.

The level of microdeformations in NCs synthesized from selenourea in the [112] direction with an increase in the synthesis time, decreases from $\varepsilon_{(112)} = 8.16 \times 10^{-3}$ (τ = 0 min) to $\varepsilon_{(112)} = 4.1 \times 10^{-3}$ (τ = 60 min). A similar decrease was observed (Table II) for other investigated crystallographic directions. This effect was caused by an increase in temperature and an increase in the zinc content of the precursor during the synthesis of NCs by the second method. It should be noted that when we used amorphous selenium as the Se source, the resulting NCs had larger CSR sizes and a significantly (2–4 times) lower level of microdeformation ($\varepsilon_{(112)} = 4.07 \times 10^{-3}$–$8.16 \times 10^{-3}$) compared to that obtained using selenourea ($\varepsilon_{(112)} = 1.55 \times 10^{-3}$–$2.27 \times 10^{-3}$). Since both the CSR boundaries and microdeformations in the material are due to the presence of dislocations, increasing L and decreasing ε should lead to a decrease in the density of dislocations in films, which will subsequently be created with the synthesized NCs [75–77].

3.2. Optical properties of Cu_2 $ZnSnSe_4$ NCs

3.2.1. FTIR spectra

The Fourier transform infrared spectroscopy (FTIR) spectra from NCs, taken in the mode of full reflection of light at room temperature, are shown in Fig. 5. FTIR absorption spectra were measured to identify the chemical bonds in the investigated samples [78]. As can be seen, the absorption bands are observed at the frequencies 3741, 3421, 2558, 2164, 2037, 1979, 1647, 1165, and 1068 cm^{-1}. It should be noted that the $Cu_2ZnSnSe_4$ kesterite phase's active IR oscillations were not detected in the measured range due to their location at lower wavelengths (50–400 cm^{-1}) [79].

Therefore, particular attention was paid to the identification of residues of organic surfactants and solvents used in the synthesis of NCs. As shown by the spectra analysis, the absorption bands at 3741 cm^{-1} and 1647 cm^{-1} can be associated with the valence vibrations of the O–H bonds and the H–O–H oscillation group, respectively [80]. The appearance of these bands indicates the presence of water residues in the nanocrystals. The peak at a frequency of 1068 cm^{-1} relates to the CO_2 carbonate group that was formed by carbon dioxide in the air [81]. The band at 2558 cm^{-1} relates, in turn, to the S–H oscillation group. The most pronounced

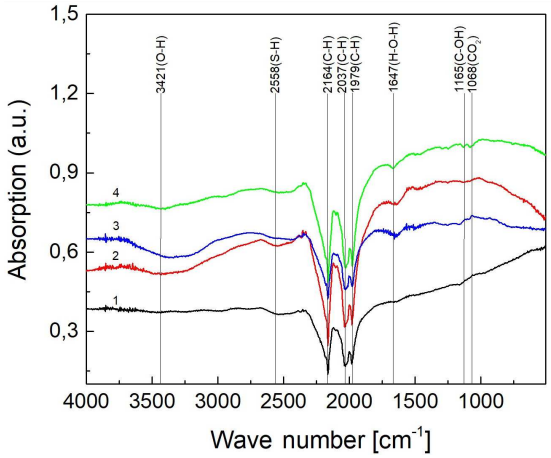

Fig. 5. FTIR spectra of $Cu_2ZnSnSe_4$ NCs from 500 to 4000 cm^{-1} at T = 260°C, τ = 120 min, selenium source — elemental Se, precursor composition — 2:1:1:4 (1); T = 280°C, τ = 120 min, Se, 2:1.5:1:4 (2); T = 280°C, τ = 120 min, Se, 2:1.8:1:4 (3); T = 240°C, τ = 30 min, $(NH_2)_2CSe$; 2:1:1:4 (4).

absorption bands at the frequencies 2164, 2037, and 1979 cm^{-1} relate to the C–H group due to the use of organic matter in the synthesis of NCs. The peak at 1165 cm^{-1} is associated with the stretched C–OH bonds. Thus, the studied samples mainly contain residues of the substances used in their synthesis.

3.2.2. Raman spectra

The XRD method cannot adequately confirm the formation of the pure kesterite phase in $Cu_2ZnSnSe_4$ NCs because of the positions of the diffraction peaks on the diffraction patterns and the lattice parameters of the four-component compound, as well as the fact that some possible impurity phases ZnSe, Cu_2Se, Cu_2SnSe_3 are similar [82]. Therefore, to establish the formation of kesterite in the samples, the synthesized NCs under optimal conditions were analyzed using Raman spectroscopy.

Figure 6 shows Raman spectra of $Cu_2ZnSnSe_4$ NCs synthesized from a solution containing amorphous selenium. These spectra have peaks at offset frequencies 168, 180, 188, 231, and 252 cm^{-1}. The peaks at 180 cm^{-1} and 188 cm^{-1} have the largest intensity. The presence of a low-intensity peak at a frequency of 204 cm^{-1} is also possible.

It is known that the spectrum of $Cu_2ZnSnSe_4$ is similar to this of Cu_2ZnSnS_4 and contains three peaks, i.e., the most intense one at 195–196 cm^{-1} and two less intense at frequencies 172–174 cm^{-1} and 233–238 cm^{-1} [83]. Thus, in our opinion, the peaks at the offset frequencies 168 and 188 cm^{-1} belong to the compound $Cu_2ZnSnSe_4$. The shift of the position of the lines in the spectrum in relation to the position characteristic of the bulk material is related to the nanoscale shape of the studied particles. The peak at a frequency of 231 cm^{-1} also belongs

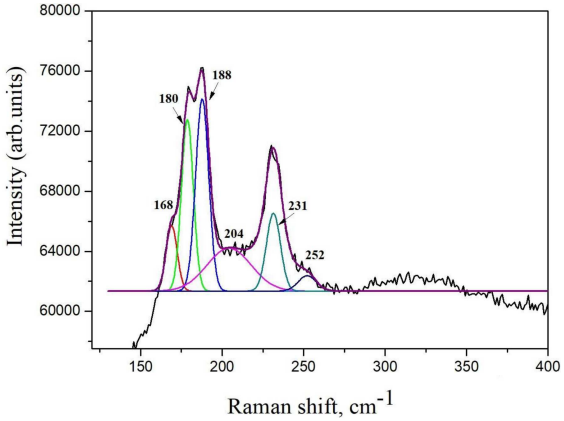

Fig. 6. Raman spectra from $Cu_2ZnSnSe_4$ nanocrystals synthesized at $T = 280°C$, $\tau = 120$ min for non-stoichiometric precursors 2:1.8:1:4.

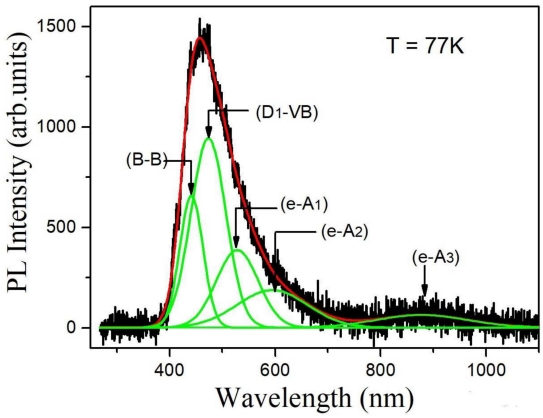

Fig. 7. PL spectrum of $Cu_2ZnSnSe_4$ NCs obtained at $T = 77$ K using excitation by LED with $\lambda = 274$ nm (4.53 eV).

TABLE III

The Raman frequencies for selenium-containing compounds.

Compound	Structure	Raman shift [cm^{-1}] [84]
Experimental data		
$Cu_2ZnSnSa_4$	kesterite/stanite	168, 188, 231
Cu_2SnSa_3	cubic	180
ZnSe	wurtzite	204, 252
Reference data		
$Cu_2ZnSnSa_4$	kesterite/stanite	174, 195, 233
Cu_2SnSa_3	cubic	180, 200, 236, 252
ZnSe	wurtzite	206, 250
SnSe	orthorhombic	33, 71, 108, 130, 150
$SnSe_2$	hexagonal	119, 185
$\alpha-Se$	amorphous	255
MoSe	hexagonal	245, 284
$Cu_{2-x}Se$	cubic/hexagonal	91, 260–270
Se_8	trigonal	143, 237

to this compound and, unlike the previous ones, it almost did not shift in frequency compared to the massive substance. The $Cu_2ZnSnSe_4$ nanocrystals contain some additional phase that gives a peak at frequencies of 180, 204, and 252 cm^{-1}. The first maximum is usually observed in the spectra of the Cu_2SnSe_3 compound and the next two — the ZnSe compound (Table III). Thus, the synthesized particles are most likely biphasic and contain a low concentration of secondary phases.

3.2.3. Photoluminescent studies

It is well known that the method of low-temperature photoluminescence (PL) is a highly sensitive non-destructive method of detecting the secondary phases in kesterite compounds [85]. In this work, in order to identify such phases, studies of the PL spectra of nanoparticles (NPs) synthesized under optimal conditions were performed. Measurements were carried out at $T = 77$ K using excitation sources of different energy.

Figure 7 shows the PL spectrum of $Cu_2ZnSnSe_4$ NPs using excitation by LED with $\lambda = 274$ nm (4.53 eV) and its decomposition into the number of lines. As can be seen in Fig. 7, the most intense PL band has two components, i.e., at 441.4 nm (2.809 eV) and 473.5 nm (2.619 eV). The short-wavelength component may be due to exciton or band–band (B-B) transitions characteristic of the ZnSe compound. While the other component at 473.5 nm may be due to recombination processes involving relatively shallow defect centers, which may be a donor-type centers (D_1 — VB transitions). The appearance of such a donor center may be due to the presence of interstitial zinc atoms, which leads to the formation of a donor level with ionization energy of 220 meV [86].

It should also be noted that band showed on Fig. 7 has a long-wavelength edge stretched to 750 nm (1.65 eV). This indicates that other PL bands may also appear in this spectral region. According to the decomposition results of the PL spectrum presented in Fig. 7, we can also observe additional bands at 528.3 nm (2.347 eV) and 601.4 nm (2.062 eV). Such bands associated with defects can be observed in particular as a result of their resonant excitation, i.e., when the excitation energy is less than the bandgap of the material. Thus, according to [87], the ZnSe compound is characterized by the appearance of PL bands in the green and red regions of the spectrum. The appearance of these bands is due to recombination processes involving copper — namely neutral $Cu^{\bullet}_{Zn}$ and single-charged Cu^{-}_{Zn} centers. The presence of this type of defects in the ZnSe secondary phase in $Cu_2ZnSnSe_4$ NPs is quite probable because Cu is one of the kesterite components. Copper atoms form deep acceptor centers in ZnSe with ionization energy of 0.73 eV. In the case of the neutral center $Cu^{\bullet}_{Zn}$, its energy is 0.35 eV [87]. As can be seen in Fig. 7, the investigated PL spectrum contains two bands in the green and red regions of the spectrum at energies

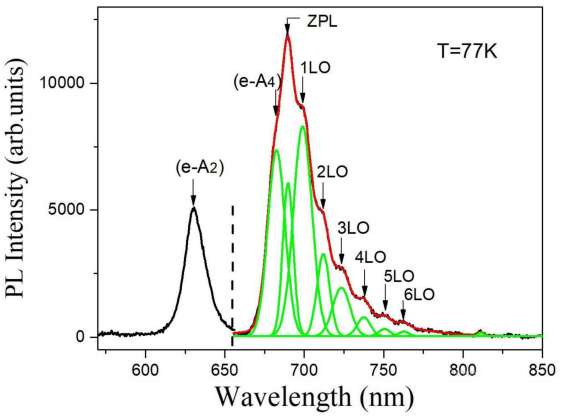

Fig. 8. PL spectrum of $Cu_2ZnSnSe_4$ NPs obtained at $T = 77$ K using excitation by LED with $\lambda = 620$ nm (1.99 eV).

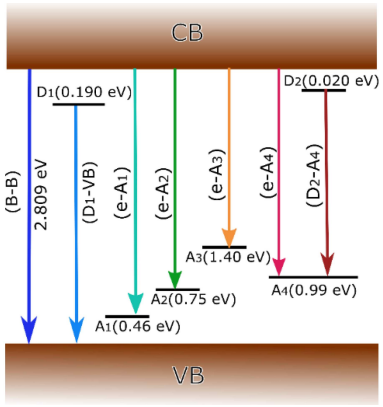

Fig. 9. Energy band scheme with the expected energy states associated with defects in the secondary phase of ZnSe.

of (528.3 nm) 2.347 eV and (601.4 nm) 2.062 eV, respectively. This means that there are two acceptor levels (A_1 and A_2) with ionization energies of 0.46 eV and 0.75 eV, associated with defect centers caused by the presence of Cu atoms in ZnSe. Therefore, the PL bands at 528.3 nm and 601.4 nm correspond to the (e–A_1) and (e–A_2) optical transitions. It should be noted that the PL spectrum also shows a low-intensity band at 875 nm (1.417 eV), which may be associated with photoionization processes involving a deeper defect level (A_3 acceptor), the nature of which remains unknown. In this case, the optical transitions (e–A_3) take place.

For ZnSe crystals, PL can also be observed under optical excitation, the energy of which is lower than the bandgap energy. In this case, resonant excitation of defect states may occur, resulting in their participation in PL. One may expect optical transitions between one of the energy bands and the defect level or transitions involving donor and acceptor levels, the so-called PL of donor–acceptor pairs. Therefore, it is of interest to conduct studies of low-temperature PL spectra under optical excitation, the energy of which is lower than the value of E_g for the given semiconductor material. For our case, we used excitation by LED with a wavelength of 620 nm. The obtained PL spectrum is shown in Fig. 8.

As can be seen in Fig. 8, two bands are observed in the PL spectrum at 630 nm (1.97 eV) and 689 nm (1.80 eV). The energy of the short-wavelength band practically coincides with the energy of the optical transition with the participation of a single-charged Cu^-_{Zn} acceptor center (A_2) and the conduction band. Therefore, such a PL band can be the result of recombination processes involving free electrons and holes localized at the acceptor levels of copper impurity centers. In this case, there is an almost resonant excitation of such impurity centers. The other band at the energy of 1.80 eV is apparently due to radiative recombination of the donor–acceptor pairs. It should be noted that a characteristic feature of PL associated with radiative recombination of donor–acceptor pairs is the participation of longitudinal–optical (LO) phonons in such processes. The decomposition of this band into a number of lines shows that its long-wavelength wing contains a number of equidistant PL bands. The energy distance between adjacent bands is, on average, about 30.5 meV. The magnitude of this energy is very close to the LO-phonon energy for ZnSe crystals, which is 31 meV [88]. The presence of the detected structure of the PL spectrum indicates that its nature results from the radiation of the donor–acceptor pairs in the ZnSe compound and thus confirms the presence of the corresponding secondary phase in $Cu_2ZnSnSe_4$ nanocrystals. In this case, the PL band at 1.80 eV can be considered a zero-phonon line (ZPL). As shown in Fig. 8, the PL band also contains an additional component on its short-wavelength edge at 682.3 nm (1.817 eV). The appearance of this band indicates that it can be due to the recombination of free electrons in the conduction band and holes of the deep acceptor center with an ionization energy of 0.99 eV (A_4 acceptor). The presence of a deep acceptor center may be due to the presence of impurity Sn atoms in ZnSe. Typically, such impurity atoms form deep levels in A^2B^6 semiconductors [89]. In this case, the ionization energy of the shallow donor level is 20 meV, which may be due to once positively charged selenium vacancies, the depth of which is ≈ 0.02 eV [90]. Based on the results of studies of the PL spectra, an energy band scheme with the expected energy states associated with defects in ZnSe was constructed (see Fig. 9).

It should be noted that this phase is practically not fixed by Raman spectroscopy. The ZnSe phase usually gives peaks at 206 cm^{-1} and 250 cm^{-1}, but in the Raman spectra, the first peak and replaced by the second. However, on closer inspection, one can see a peak of very low intensity. Such a difference in the manifestation of LO-phonons may be due to the different sensitivity of the methods used.

4. Conclusion

1. This work proposes a new procedure for the polyol synthesis of NCs of the $Cu_2ZnSnSe_4$ compound, where amorphous selenium is used as the Se source. The following optimal synthesis conditions are selected: temperature (T=280°C), time (τ=120 min), and the molar ratio of the components in the precursor (2:1.5:1:4), in which the crystals had a single-phase structure of the kesterite type and the composition (C_{Cu} = 29.0 at.%, C_{Zn} = 12.1 at.%, C_{Sn} = 12.7 at.%, C_{Se} = 46.2 at.%) close to the stoichiometric. The use of elemental selenium for the synthesis made it possible to significantly reduce the costs of obtaining the compound.
2. We compared the structural (phase composition, crystal lattice parameters, unit cell volume) and substructural (CSR sizes, level of microdefromations) properties of $Cu_2ZnSnSe_4$ NCs obtained by synthesis using selenourea as a source of Se (which is traditional in such cases) in the first approach, and amorphous selenium in the second approach.
3. Using the UnitCell program and the position of the diffraction reflection from the [112] crystallographic plane, we determined the lattice parameters of the synthesized crystals. It was found that although the values of the unit cell constants of the material found by two different methods differed significantly in magnitude, the general form of the dependence of a, c, $c/(2a)$, V_{unit} on T, τ and the composition of precursors were similar. It was shown that the lattice parameters of NCs synthesized by the first method vary in the ranges a_{UC} = 0.56605–0.56777 nm, c_{UC} = 1.12621–1.13345 nm, $c_{UC}/(2a_{UC})$ = 0.99245–1.0009. The parameters closest to reference data a_{UC}=0.56930 nm were found in the nanocrystals synthesized at τ=45 min. For NCs synthesized by the second method, a tendency to increase the values of a, c, and V_{unit} with the increase in the synthesis temperature and the zinc content in the precursor was observed. At the same time, the ratio $c/(2a)$ decreases. The obtained results correlate well with the data given in the reference literature.
4. It was found that the size of NCs synthesized using elemental selenium as a precursor component (D = 18–30 nm) and CSR ($L_{(112)}$=16.54–24.23 nm) were much higher than when using selenourea (D = 5–12 nm, $L_{(112)}$ = 4.47–9.03 nm). At the same time, these sizes increased with increasing synthesis temperature and zinc content in the precursor. A similar increase in the CSR sizes was observed in NCs synthesized with the use of selenourea and an increase in the time of their synthesis. In both cases, the crystals CSR had a shape close to spherical.
5. It was shown that when using amorphous selenium as a source of Se, the obtained NCs had a significantly (2–4 times) lower level of microdeformations ($\varepsilon_{(112)}$ = 4.07×10^{-3}–8.16×10^{-3}) compared to that obtained using selenourea ($\varepsilon_{(112)} = 1.55 \times 10^{-3}$–$2.27 \times 10^{-3}$) thus the films based on them will contain fewer dislocation centers, which are effective recombination centers of charge carriers.
6. By the method of Raman spectroscopy in the nanocrystals obtained under optimal conditions (T=280°C, τ=120 min for nonstoichiometric precursors 2:1.5:1:4) from a precursor containing amorphous selenium, in addition to the main phase, the presence of some compounds Cu_2SnSe_3 have been observed, and by the method of low-temperature PL, also small quantities of ZnSe. Thus, to obtain fully single-phase nanocrystals, the samples require further annealing.
7. Synthesized $Cu_2ZnSnSe_4$ NCs dispersed in an environmentally friendly mixture of water, glycol, alcohol, and polyvinylpyrrolidone can be used for 2D and 3D printing of films from a four-component compound, used as absorbers of third-generation solar cells, active layers of thermogenerators and other electronic devices.

Acknowledgments

The research was performed under the financial support of the Ministry of Education and Science of Ukraine (0122U000787). This work was also supported by PROJECT NATO SPS, MYP (project registration number: G5916).

References

[1] A.H. Espera, J.R.C. Dizon, Q. Chen, *Prog. Addit. Manuf.* **4**, 245 (2019).

[2] R. Yang, J. Zhou, C. Yang, L. Qiu, H.-M. Cheng, *Adv. Mater. Technol.* **5**, 1901066 (2020).

[3] Z. Zhu, D.W.H. Ng, H.S. Park, *Nat. Rev. Mater.* **6**, 27 (2020).

[4] H. Yang, W.R. Leow, X. Chen, *Small Methods* **2**, 1700259 (2018).

[5] B.S. Cook, B. Tehrani, J.R. Cooper, S. Kim, M. Tentzeris, in: *Handbook of Flexible Organic Electronics*, Ed. S. Logothetidis, Woodhead Publishing, Oxford 2015, p. 199.

[6] Q. Huang, Y. Zhu, *Adv. Mater. Technol.* **4**, 1800546 (2019).

[7] W. Zhu, S. Park, M. Yogeesh, D. Akinwande, *Flex. Print. Electron.* **2**, 043001 (2017).

[8] K.S. Kumar, P.Y. Chen, H. Ren, *Research* **2019**, 3018568 (2019).

[9] V. Chi-Fung Li, X. Kuang, C.M. Hamel, D. Roach, Y. Deng, H. Jerry Qi, *Addit. Manuf.* **28**, 14 (2019).

[10] G. Siqueira, D. Kokkinis, R. Libanori, M.K. Hausmann, A. S. Gladman, A. Neels, P. Tingaut, T. Zimmermann, J. A. Lewis, A. R. Studart, *Adv. Funct. Mater.* **27**, 1604619 (2017).

[11] I.J. Fernandes, A.F. Aroche, A. Schuck, *Sci. Rep.* **10**, 8878 (2020).

[12] L. Nayak, S. Mohanty, S. Nayak, A. Ramadoss, *J. Mater. Chem.* **29**, N7 (2019).

[13] B. Begines, A. Alcudia, R. Aguilera-Velazquez, *Sci. Rep.* **9**, 16097 (2019).

[14] T. Jie, Z. Jiumeng, D. Ting, X. Xin, D. Xianming, C. Shaochen, L. Jinlu, C. Yuwen, L. Xuan, X. Meimei, L. Yi, Hao Cheng, M. Jian, Ludwig Cardon, G. Maling, W. Yuquan, *Acta Biomater.* **90**, 49 (2019).

[15] C. Liu, N. Huang, F. Xu, J Tong, Z. Chen, X. Gui, Y. Fu, C. Lao, *Polymers* **10**, 629 (2018).

[16] T.E. Glier, L. Akinsinde, M. Paufler, *Sci. Rep.* **9**, 6465 (2019).

[17] Y. Liu, Y. Xu, R. Avila, C. Liu, Z. Xie, L. Wang, X. Yu, *Nanotechol.* **30**, 41400 (2019).

[18] J. Hoerber, J. Glasschroeder, M. Pfeffer, J. Schilp, M. Zaeh, J. Franke, *Proc. CIRP* **17**, 806 (2014).

[19] Y. Dong, C. Bao, W. Soo Kim, *Joule* **2**, 579 (2018).

[20] J.J. Cabrera-López, M.F. García-Arrunátegui, P. Neuta-Arciniegas, O. Campo, J. Velasco-Medina, *J. Phys. Conf. Ser.* **1272**, 012017 (2019).

[21] H. W. Tan, J. An, C.K. Chua, T. Tran, *Adv. Electron. Mater.* **5**, 1800831 (2019).

[22] S. Ganesan, S. Mehta, D. Gupta, *Opto-Electron. Rev.* **27**, 298 (2019).

[23] S.K. Karunakaran, A.G. Manohari, W.G. Yang, S. Khanib, X. Lin, G. Yang, *J. Mater. Chem. A.* **7**, 13873 (2019).

[24] J. Peng, I. Witting, N. Geisendorfer, *Nat. Commun.* **10**, 5590 (2019).

[25] F. Kim, B. Kwon, Y. Eom et al., *Nat. Energy* **3**, 301 (2018).

[26] M.R. Burton, S. Mehraban, D. Beynon, J. Mc Gettrick, T. Watson, N.P. Lavery, M.J. Carnie, *Adv. Energy Mater* **9**, 1900201 (2019).

[27] N. Bandari, J. Dargahi, M. Packirisamy, *IEEE Access* **8**, 7682 (2020).

[28] Y. Ni, R. Ji, K. Long, T. Bu, K. Chen, S. Zhuang, *Appl. Spectrosc. Rev.* **52**, 623 (2017).

[29] M. R. Khosravani, T. Reinicke, *Sens. Actuators A Phys.* **305**, 111916 (2020).

[30] Z. Minxiang, Z. Yanliang, *J. Mater. Chem. A* **41**, 9 (2019).

[31] S. Hwan, J. Chung, N. Hotz, K. Hyun, C. Grigoropoulos, *J. Micromech. Microeng.* **20**, 125010 (2010).

[32] N. Honglong, T. Ruiqiang, Y. Rihui, C. Jianqiu, Y. Caigui, Z. Yicong, C. Wei, Z. Zhennan, P. Junbiao, *Mater. Rep.* **32**, 2959 (2018).

[33] M.A. Green, Y. Hishikawa, W. Warta, *Prog. Photovolt.* **30**, 3 (2021).

[34] K. Ito, in: *Copper Zin Tin Sulfide-Based Thin Film Solar Cell*, John Wiley & Sons, Chichester 2015, p. 440.

[35] H. Katagiri, K. Saitoh, T. Washio, *Sol. Energy Mater. Sol. Cells* **65**, 141 (2001).

[36] S. Giraldo, Z. Jehl, M. Placidi, V. Izquierdo-roca, A. Perez-rodriguez, E. Saucedo, *Adv. Mater.* **31**, (2019) 1806692.

[37] X. Liu, Y. Feng, H. Cui, F. Liu, X. Hao, G. Conibeer, D.B. Mitzi, M. Green, *Prog. Photovolt.* **24**, 879 (2016).

[38] A.S. Nazligul, M. Wang, K.L. Choy, *Sustainability* **12**, 5138 (2020).

[39] P. Krishan, S. Pawan, B. Abhishikta, B.T. Khem, *Sol. Energy Mater. Sol. Cells* **196**, 138 (2019).

[40] M. Ravindiran, C. Praveenkumar, *Renew. Sustain. Energy Rev.* **94**, 317 (2018).

[41] T. Ratz, G. Brammertz, R. Caballero et al., *J. Phys. Energy* **1**, 42003 (2019).

[42] Z. Shi, D. Attygalle, A.H. Jayatissa, *J. Mater. Sci. Mater Electron.* **28**, 2290 (2017).

[43] F. Martinho, S. Marino, M. Espindola et al., *ACS Appl. Mater. Interfaces* **12**, 39405 (2020).

[44] M.A. Green, E.D. Dunlop, J. Hohl-Ebinger, M. Yoshita, N. Kopidakis, X. Hao, *Prog. Photovolt. Res. Appl.* **28**, 629 (2020).

[45] T. Gokmen, O. Gunawan, T. Todorov, D.B. Mitzi, *Appl. Phys. Lett.* **103**, 103506 (2013).

[46] M. Suryawanshi, G. Agawane, S.M. Bhosale, S.W. Shin, P. Patil, K. Jeong-Hoon, A. Moholkar, *Mater. Technol.* **28**, 98 (2013).

[47] J. Wang, J. Hu, Y. Guo, *NPG Asia Mater.* **4**, e2 (2012).

[48] C. Leidholm, C. Hotz, A. Breeze, C. Sunderland, W. Ki, D. Zehnder, *Final Report: Sintered CZTS Nanoparticle Solar Cells on Metal Foil*, NREL/SR-5200–56501, National Renewable Energy Laboratory, 2012.

[49] M. Huang, H.S. Zheng, A.X. Wei, *J. Mater. Sci. Mater. Electron.* **29**, 8049 (2018).

[50] P. Mou, N.R. Mathews, R. Silva Gonzalez, X. Mathew, *Thin Solid Films* **535**, 78 (2013).

[51] Y. Li, Q. Han, T. W. Kim, W. Shi, *Nanoscale* **6**, 3777 (2014).

[52] R. Chalapathy, S. Das, J.S. Ma, J.C. Sung, C.H. Lu, *J. Mater. Sci. Mater. Electron.* **26**, 7673 (2015).

[53] W. Lu, S. Yiling, X. Yong, in: *Proc. 2016 4th Int. Conf. on Advanced Materials and Information Technology Processing (AMITP 2016)*, 2016, p. 499.

[54] K. Liu, N. Ji, L. Shi, H. Liu, *J. Nanomater.* **2014**, 910639 (2014).

[55] C. Jin, P. Ramasamy, J. Kim, *Dalton Trans.* **43**, 9481 (2014).

[56] M. Ibáñez, T. Berestok, O. Dobrozhan, *J. Nanopart. Res.* **18**, 226 (2016).

[57] C. Wang, S. Shei, S. Chang, *Opt. Mater. Express.* **4**, 1593 (2014).

[58] C. Wang, S. Shei, S. Chang, *IEEE Trans. Nanotechnol.* **14**, 896 (2015).

[59] O. Dobrozhan, M. Baláž, S. Vorobiov, P. Baláž, A. Opanasyuk, *J. Alloys Compd.* **842**, 155883 (2020).

[60] S. Kakherskyi, O. Dobrozhan, R. Pshenychnyi, D. Kurbatov, N. Opanasyuk, in: *2020 IEEE 40th Int. Conf. on Electronics and Nanotechnology (ELNANO)*, IEEE, Kyiv 2020.

[61] P. Baláž, M. Hegedus, M. Baláž, O. A. Dobrozhan, *Prog. Photovolt. Res. Appl.* **27**, 798 (2019).

[62] O. Dobrozhan, I. Shelest, A. Stepanenko, D. Kurbatov, M. Yermakov, A. Čerškus, S. Plotnikov, A. Opanasyuk, *Materials Science in Semiconductor Processing* **108(15)**, 104879 (2020).

[63] O.A. Dobrozhan, P.S. Danylchenko, D.I. Kurbatov, N.M. Opanasyuk, A.S. Opanasyuk, in: *2017 IEEE 7th Int. Conf. Nanomaterials: Application & Properties (NAP)*, IEEE, Odessa 2017.

[64] G. Chen, C. Yuan, J. Liu, Y. Deng, G. Jiang, W. Liu, C. Zhu, *J. Power Sources* **262**, 201 (2014).

[65] C. Ritchie, A.S.R. Chesman, J. Jasieniak, P. Mulvaney, *Chem. Mater.* **31**, 2138 (2019).

[66] Y. Li, Q. Han, T. Kim, W. Shi, *Nanoscale* **6**, 3777 (2014).

[67] W. Wong-Ng, H.F. McMurdie, C.R. Hubbard, A.D. Mighell, *J. Res. Natl. Inst. Stand. Technol.* **106**, 1013 (2001).

[68] O. Dobrozhan, V. Loboda, Ya. Znamenshchykov, A. Opanasyuk, H. Cheong, *J. Nano- Electron. Phys.* **9**, 01028 (2017).

[69] O. Dobrozhan, O. Diachenko, M. Kolesnyk, A. Stepanenko, S. Vorobiov, P. Baláž, S. Plotnikov, A. Opanasyuk. *Mater. Sci. Semicond. Process.* **102**, 104595 (2019).

[70] V. Kosyak, A. Voznyi, P. Onufrijevs, L. Grase, J. Vecstaudža, A. Opanasyuk, A. Medvids, G. Mezinskis, *J. Alloys Compd.* **688**, 130 (2016).

[71] V. Kosyak, Y. Znamenshchykov, A. Čerškus, E. Dauksta, Y. Gnatenko, L. Grase, J. Vecstaudza, A. Medvids, A. Opanasyuk, G. Mezinskis, *J. Alloys Compd.* **682**, 543 (2016).

[72] S. Kakherskyi, R. Pshenychnyi, O. Dobrozhan, J. Vaziev, A.P. Bukivskii, P.M. Bukivskij, Y.P. Gnatenko, A. Opanasyuk, *Appl. Phys. A* **127**, 715 (2021).

[73] S. Ji, T. Shi, X. Qiu, *Sci. Rep.* **3**, 2733 (2013).

[74] S.A. Vanalakar, G.L. Agawane, A.S. Kamble, *Appl. Phys. A* **123**, 782 (2017).

[75] Y. Yawei, Q. Wenxiu, Z. Xinyu, Y. Xingtian, X. Yonglei, Q. Meidan, Z. Hongyang, D. Yaping, *Appl. Catal. B* **200**, 402 (2017).

[76] Y. Cao, C. Wang, J. Hu, *Adv. Mater. Res.* **347–353**, 848 (2011).

[77] T. Wang, Q. Chen, J. Chen, F. Zhou, Z. Jia, X. Dou, S. Zhuang, *Cryst. Res. Technol.* **49**, 808 (2014).

[78] S.-H. Hsiao, Y.-T. Chou, *Polymer* **55**, 2411 (2014).

[79] M. Himmrich, H. Haeuseler, *Spectrochim. Acta* **47**, 933 (1991).

[80] K. Kaviyarasu, D. Premanand, J. Kennedy, E. Manikandan, *Int. J. Nanosci.* **12**, 1 (2013).

[81] Mohammad Shiri, H. Aghazadeh, M. Synthesis, *Nanopart. J. Electrochem. Soc.* **159**, E132–E138. (2012).

[82] H. Flammersberger, M.Sc. Thesis, Uppsala University 2010.

[83] D.B. Mitzi, O. Gunawan, T.K. Todorov, K. Wang, S. Guha, *Sol. Energy Mater. Sol. Cells* **95**, 1421 (2011).

[84] P.M.P. Salomé, P.A. Fernandes, J.P. Leitão, *J. Mater. Sci.* **49**, 7425 (2014).

[85] M. Grossberg, J. Krustok, K. Timmo, M. Altosaar, *Thin Solid Films* **517**, 2489 (2009).

[86] D.B. Laks, *Phys. Rev.* **45**, 10965 (1992).

[87] G.B. Stringfellow, R.H. Bube, *Phys. Rev.* **171**, 903 (1968).

[88] M. Dimitrievska, H. Xie, A.J. Jackson, X. Fontané, M. Espındola-Rodrıguez, E. Saucedo, A. Perez-Rodrıguez, A. Walshband, V. Izquierdo-Roca, *Phys. Chem. Chem. Phys* **18**, 7632 (2016).

[89] R.V. Gamernyk, Yu.P. Gnatenko, P.M. Bukivskij, P.A. Skubenko, Y.Yu. Slivka, *J. Physics: Condens. Matter* **18**, 5323 (2006).

[90] I. Abbasov, M. Musayev, J. Huseynov, M. Kostyrko, S. Babayev, G. Eyyubov, S. Aliyeva, *Ukr. J. Phys. Opt.* **21**, 103 (2020).